

The new generation lunar gravitational wave detectors: sky map resolution and joint analysis

Xiaolin Zhang,^{1,*} Chengye Yu,^{1,†} Haoran Li,^{1,‡} Sobhan Kazempour,^{1,§} Mingqiu Li^{1,¶} and Sichun Sun^{1,**}

¹*School of Physics, Beijing Institute of Technology, Beijing, 100081, China*

(Dated: December 30, 2025)

Lunar-based gravitational-wave interferometry is a fascinating endeavor, and was proposed as a promising approach to bridge the observational gap between space-borne and ground-based detectors. In this work, we adopt the Fisher-matrix method to examine the angular-resolution performance of the newly proposed Crater Interferometry Gravitational-wave Observatory (CIGO) on the lunar crater rim near the north pole, together with TianQin and LISA, for monochromatic sources in the 0.1–10Hz band. We find that above 0.1Hz, CIGO achieves better localization accuracy than the other two space-based missions and dominates the combined detector network’s performance, provided that lunar noise mitigation is achieved in the 0.1–2.87 Hz frequency range. We further explore an upgraded Tetrahedron configuration, TCIGO, with a fourth station at the bottom of a crater, which forms a regular tetrahedral constellation on the lunar surface. The result shows that TCIGO yields a five-fold improvement in angular-resolution capability over CIGO and gets better sky coverage across the target frequency band.

I. INTRODUCTION

Gravitational-wave (GW) detection has become a crucial method of probing the nature of compact astrophysical objects under extreme conditions. Gravitational waves (GWs) cover a broad frequency range from 10^{-16} to 10^4 Hz. [1–3] Existing GW detection missions are designed to probe different segments of this spectrum. Ground-based detectors, such as LIGO and Virgo[4–11], are sensitive to frequencies in the range of 3 Hz– 2×10^4 Hz, while space-based interferometers like LISA [12, 13] TianQin[14, 15] and Taiji [16, 17]target the lower-frequency band of 10^{-4} – 10^{-1} Hz. However, the intermediate deci-hertz range (0.1–10 Hz) lies outside the optimal sensitivity bands of both ground- and space-based detectors.

The deci-hertz window (0.1–10 Hz) is of particular astrophysical interest, as it encompasses numerous rich phenomena[18, 19], such as the mergers of intermediate-mass black holes, compact binary white dwarf systems, and core-collapse supernovae[20–22]. Moreover, it provides a unique opportunity to test General Relativity [23, 24]and extensions of the Standard Model [25–28]. Thus, constructing detectors optimized for this frequency range is essential for probing these processes.

Several proposals have been put forward for **space-based** deci-hertz GW observatories to bridge this gap, including the geocentric mission like SAGE[20] and heliocentric concepts such as DECIGO[29, 30], TVLBAI[31] and ALIA [32],and for **earth-based** detectors including TOBA[33],AION[34]and ZAIGA[35]. Recently, lunar-based GW detection has attracted increasing attention, aiming to fill this observational blind spot[29, 31, 36–41]. The **lunar** GW observatory concept envisions the construction of an interferometric detector on the Moon. GLOC[42]and LILA[43] missions were proposed, aiming to build a 40-km equilateral triangle laser interferometer on the lunar surface as part of NASA’s Artemis program. LGWA deploys an array of high-end seismometers on the Moon to monitor its normal modes in the 1 mHz–1 Hz band excited by GWs [40, 44, 45]. Additionally, Italian researchers proposed the LSGA project to detect GW-induced lunar seismic strains.[44, 45]

There are a few advantages to constructing GW detectors on the Moon. Compared with **Earth-based** detectors, firstly, the Moon naturally provides an ultra-high-vacuum environment, with surface pressures as low as 10^{-8} Pa at sunrise, comparable to the LIGO vacuum system, significantly reducing construction and maintenance costs[46]. Secondly, at low frequencies (0.1–0.4 Hz), lunar seismic noise is three to four orders of magnitude lower than that on Earth[42, 47]. Thirdly, the absence of atmospheric, human, and tectonic disturbances allows for stable, long-term operation with a high duty cycle[43, 48, 49]. Consequently, gravity-gradient noise is also strongly suppressed, thereby minimizing the need for costly mitigation strategies[31, 37–41]. Compared with **space-based** detectors, a lunar-based GW observatory, stationed on the surface, can be serviced directly by astronauts, resulting in far lower maintenance

* xiaolinzhang66@outlook.com

† chengyeyu1@hotmail.com

‡ lee.haoran@outlook.com

§ sobhan.kazempour1989@gmail.com

¶ limingqiu17@mails.ucas.ac.cn

** sichunssun@gmail.com

costs than those of deep space missions. Secondly, for low-frequency signals around 0.1 Hz, the data transmission rate required for a lunar observatory is only about one order of magnitude higher than that of space-based missions, making data transfer considerably more manageable[29, 36, 50, 51]. Together, these advantages make the Moon an auspicious site for next-generation gravitational-wave astronomy, offering a stable, low-noise, and serviceable platform that bridges the spectrum gap between ground and space-based detectors.

Several leading research institutions, including the Beijing Institute of Technology and the Chinese Academy of Sciences, in the rapid development of China's lunar exploration program, have jointly proposed an innovative concept for lunar-based gravitational-wave (GW) detection, the **Crater Interferometry Gravit-wave Observatory (CIGO)**. As a third-generation GW detector, CIGO aims to achieve a strain sensitivity of $\sim 10^{-24}$, an order-of-magnitude improvement over current second-generation detectors ($\sim 10^{-23}$). The detector is designed to operate in the frequency band of 0.1–10 Hz with an arm length of about 100 km, and is planned to be constructed in a polar lunar crater.

In this work, we focus on the monochromatic gravitational waves, which can be emitted in the early stage of compact binary systems, including intermediate-mass black holes and neutron stars[20–22, 40], the first-order phase transitions from early universe[52] and the subsequent cosmic string [53]. As with space-based detectors, we adopt an equilateral triangular configuration (see Fig. 1). Using the *Fisher Information Matrix (FIM)* method, we analyze 3600 potential GW sources distributed across the celestial sphere to evaluate the angular resolution of the detector. We further generate sky maps of localization accuracy for CIGO, LISA, and TianQin at three representative frequencies: 0.1, 1, and 10 Hz. By comparing these results, we investigate the performance of the detectors across the 0.1–10 Hz band. Besides, we compute the joint angular-resolution maps for the CIGO–LISA and CIGO–TianQin network configurations at the same frequencies, assessing the enhanced localization capability with a lunar–space joint analysis. Additionally, we upgrade the CIGO system by adding a detector at the base of the crater, forming a tetrahedral configuration with the origin plane. We then calculate and compare its angular resolution over the sky region. These results provide valuable insight into the potential of lunar-based interferometers to bridge the existing detection gap between space-based and ground-based GW observatories.

The paper is organized as follows: in Sec. II, we outline the Fisher information matrix formalism for monochromatic gravitational waves and derive the orbital configuration of the CIGO detectors; in Sec. III, we present the sky-localization performance of CIGO operating both independently and in a network with LISA, TianQin, and Taiji, and estimate the impact of lunar-based noise on CIGO's localization accuracy; in Sec. IV, we investigate the regular tetrahedral configuration of CIGO and compare its angular resolution with that of the original planar configuration to assess potential improvements.

II. FISHER INFORMATION MATRIX METHOD

A. General GW Signal and Response in GR

In general relativity, a gravitational wave signal is described by the strain tensor

$$h_{ij}(t) = \sum_{A=+, \times} e_{ij}^A h_A(t), \quad (1)$$

where $h_A(t)$ is the GW strain amplitude in the polarization mode A , and e_{ij}^A is the corresponding polarization tensor. Then the output of the detector α is

$$s^\alpha(t) = \left[\sum_A F_A^\alpha h_A(t) \right] e^{i\phi^\alpha(t)} + n_A(t), \quad (2)$$

where $A = +, \times$ denotes the plus and cross polarizations, $n_A(t)$ is the instrumental noise, $e^{i\phi^\alpha(t)}$ is the phase modulation factor. The response function F_A^α of detector α for the polarization mode A can be written as

$$F_A^\alpha = \sum_{i,j} D_{ij}^\alpha e_{ij}^A, \quad (3)$$

where D_{ij}^α is the detector tensor for detector α , and e_{ij}^A is the GW polarization tensor. The detector tensor D_{ij} , which represents the response of the instrument to signals from specific directions, for a monochromatic gravitational wave of frequency f propagating along $\hat{\omega}$, in an equal-arm Michelson laser interferometer with single round-trip light travel,

is given by

$$D_{ij} = \frac{1}{2} [\hat{u}_i \hat{u}_j T(f, \hat{\omega}) - \hat{v}_i \hat{v}_j T(f, \hat{\omega})], \quad (4)$$

respectively. The transfer function $T(f, \hat{\omega})$ is given by[54–58]

$$T(f, \hat{u} \cdot \hat{\omega}) = \frac{1}{2} \left\{ \text{sinc} \left[\frac{f(1 - \hat{u} \cdot \hat{\omega})}{2f^*} \right] \times \exp \left[\frac{f(3 + \hat{u} \cdot \hat{\omega})}{2f^*} \right] + \text{sinc} \left[\frac{f(1 + \hat{u} \cdot \hat{\omega})}{2f^*} \right] \times \exp \left[\frac{f(1 + \hat{u} \cdot \hat{\omega})}{2f^*} \right] \right\}, \quad (5)$$

where \hat{u} and \hat{v} denote the unit vectors along the two arms of the detector, and $\hat{\omega}$ is the incident direction vector of the gravitational wave (with L the arm length and c the speed of light). For CIGO, which primarily targets the 0.1–10 Hz band, the GW's wavelength is much larger than the detector arm length (100 km). This implies that the observing frequency $f \ll f^*$, so $\text{sinc}(x) \rightarrow 1$ and the transfer function approaches unity: $T(f, \hat{u} \cdot \hat{\omega}) \rightarrow 1$. Consequently, in low frequency limit, the detector tensor D^{ij} reduces to its long-wavelength, frequency-independent form:

$$D^{ij} = \frac{1}{2} (\hat{u}^i \hat{u}^j - \hat{v}^i \hat{v}^j). \quad (6)$$

The modulation factor on the detector induced by the Earth-Sun and Moon-Earth motions $e^{i\phi^\alpha(t)}$, can be expressed as follows [57]

$$e^{i\phi_D(t)} = \exp \left(2\pi i f R \cos \theta_s \cos \left(\frac{2\pi f (T - \phi_s - \phi_\alpha)}{c} \right) \right), \quad (7)$$

where f is the GW frequency, R is the orbit radius of the detector center in the heliocentric-ecliptic coordinate system. For CIGO, we can calculate using the formula:

$$R = R_E + \sin \theta_m R_M, \quad (8)$$

where R_E and R_M are the semi-major axis of Earth and Moon orbit. Due to the long duration and large scale of the CIGO mission, we often set R_E to 1 AU and the observation time T to 1 year. θ_m is the orbital inclination of the Moon in Fig.1, (θ_s, ϕ_s) is the spherical coordinates of the gravitational-wave source on the celestial sphere, ϕ_α is the ecliptic longitude of the detector α at $t = 0$. Given the significant difference in their orders of magnitude, R_M (0.00257 AU) can be neglected.

B. Lunar detector orbit and detector tensor

To calculate the detector tensor, it is necessary to determine the orbital equations of each detector (test mass) in CIGO. We adopt a heliocentric-ecliptic coordinate system (Fig. 1), centered at the solar system barycenter with the x axis pointing toward the vernal equinox, the z axis normal to the ecliptic plane, and the y axis completing the right-handed triad. The n -th detector position can be decomposed as

$$\vec{r}_n(t) = \vec{r}_E(t) + \vec{r}_M(t) + \vec{r}_n^*(t) + \vec{\epsilon}_n(t), \quad (9)$$

where $\vec{r}_E(t)$ represents the position vector of the Earth in the heliocenter frame, $\vec{r}_M(t)$ represents the position vector of the Moon relative to Earth, and $\vec{r}_n^*(t)$ represents the position vector of the detector n , where $n \in \{1, 2, 3\}$. $\vec{\epsilon}_n(t)$ is the high order perturbations correction to the orbits from the moon, the Earth, the Sun, other planets (mostly Jupiter), etc [55].

The position vector of the n -th detector is given by

$$\begin{aligned} X_n(t) &= R \sin \theta_c \cos \alpha_n(t) + R_M \cos \alpha_M(t) + R_E \cos \alpha_E(t) \\ &+ \frac{1}{2} e_1 R_M [\cos(2\alpha_M(t)) - 3] - \frac{3}{2} e_1^2 R_M \sin^2 \alpha_M(t) \cos \alpha_M(t) \\ &+ \frac{1}{2} e_2 R_E [\cos(2\alpha_E(t)) - 3] - \frac{3}{2} e_2^2 R_E \sin^2 \alpha_E(t) \cos \alpha_E(t) \\ &+ \mathcal{O}(3), \end{aligned} \quad (10)$$

$$\begin{aligned}
Y_n(t) = & \left[R \sin \theta_c \sin \alpha_n(t) + R_M \sin \alpha_M(t) + \frac{1}{2} e_1 R_M \sin(2\alpha_M(t)) \right. \\
& \left. + \frac{1}{2} e_1^2 R_M (3 \cos 2\alpha_M(t) - 1) \sin \alpha_M(t) \right] \sin \theta_m \\
& + \left[R \cos \theta_c + R_E \sin \alpha_E(t) + \frac{1}{2} e_2 R_E \sin 2\alpha_E(t) \right. \\
& \left. + \frac{1}{2} e_2^2 R_E (3 \cos(2\alpha_E(t)) - 1) \sin \alpha_E(t) \right] \cos \theta_m + \mathcal{O}(3),
\end{aligned} \tag{11}$$

$$\begin{aligned}
Z_n(t) = & R \sin \theta_m \cos \theta_c \\
& - \left[R \sin \theta_c \sin \alpha_n(t) + R_M \sin \alpha_M(t) + \frac{1}{2} e_1 R_M \sin 2\alpha_M(t) \right. \\
& \left. + \frac{1}{2} e_1^2 R_M (3 \cos 2\alpha_M(t) - 1) \sin \alpha_M(t) \right] \cos \theta_m + \mathcal{O}(3),
\end{aligned} \tag{12}$$

where $\mathcal{O}(3)$ denotes the higher-order infinitesimal to the eccentricity. Here, R is the radius of the moon; R_M and e_1 are the semi-major axis and eccentricity of the Moon's orbit around the Earth; R_E and e_2 are the semi-major axis and eccentricity of the Earth's orbit around the Sun, respectively. The angle $\alpha_n(t) = 2\pi f_n t + \kappa_n$ is the angular displacement of the n -th detector in the detector-plane-lunar polar coordinate system after time t , where $\kappa_n = 2\pi(n-1)/3$. The term $\alpha_M(t) = 2\pi f_M t + \kappa_M$ represents the mean lunar longitude of the Moon in the geocentric-lunar coordinate system, where f_M is the modulation frequency due to the Moon's orbital motion and κ_M is the mean lunar longitude at $t = 0$. Similarly, $\alpha_E(t) = 2\pi f_E t + \kappa_E$ denotes the mean ecliptic longitude of the Earth in the heliocentric-ecliptic coordinate system, where f_E is the orbital frequency of the Earth and κ_E is the mean ecliptic longitude measured from the vernal equinox at $t = 0$. $\sin \theta_c = L/R$, where L is the distance from the center of the detector to each detector. At the same time, θ_m is the angle between the lunar orbit plane and the ecliptic. The detailed derivation is provided in Appendix A.

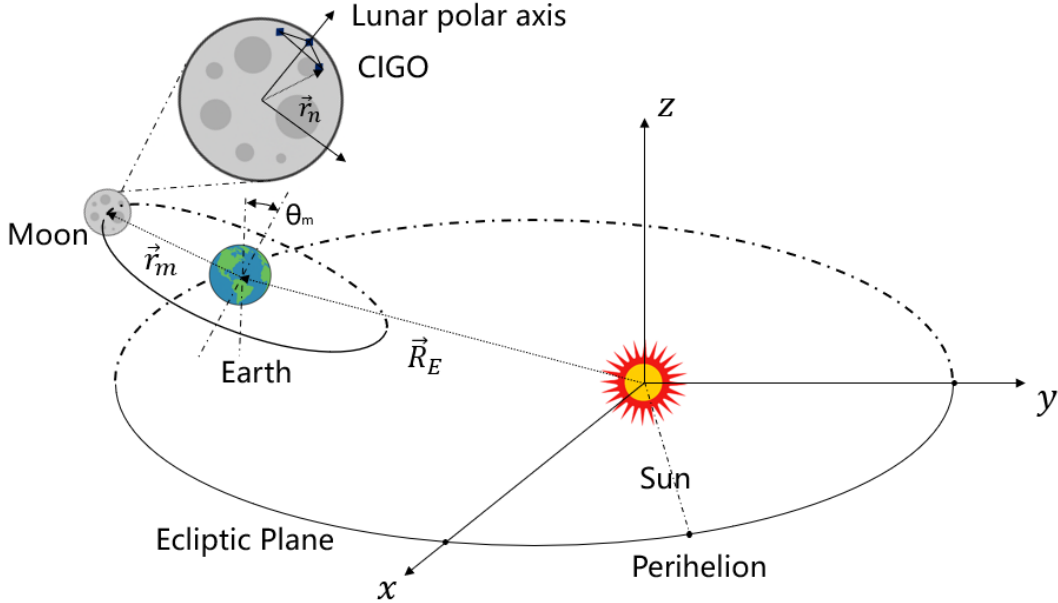


FIG. 1. Schematic diagram of CIGO's orbit and coordinate system.

C. CIGO Fisher Information Matrix Method

The monochromatic gravitational waves considered in this work can be probed by interferometers such as CIGO, as well as by other space-based detectors. At the quadrupole leading order, the two polarizations of a monochromatic

gravitational wave with frequency f_0 take the form:

$$\begin{aligned} h_+ &= \mathcal{A} \left[1 + (\hat{L} \cdot \hat{\omega})^2 \right] \exp(2\pi i f t + i\phi_0), \\ h_\times &= -2i\mathcal{A}(\hat{L} \cdot \hat{\omega}) \exp(2\pi i f t + i\phi_0), \end{aligned} \quad (13)$$

Here $\mathcal{A} = 2M_1M_2/(rd_L)$ denotes the amplitude, determined by the binary masses M_1, M_2 , the distance r between them and the luminosity distance d_L between the GW source and the observer, \hat{L} represents the unit vector for the binary's orbital angular momentum, and ϕ_0 is the initial phase. We adopt seven parameters in our Fisher information matrix (FIM) analysis:

$$\theta = (\theta_s, \phi_s, \theta_L, \phi_L, \mathcal{A}, \phi_0, f), \quad (14)$$

which are source direction (θ_s, ϕ_s) ; the direction of the binary's orbital angular momentum (θ_L, ϕ_L) ; the amplitude \mathcal{A} , the initial phase ϕ_0 , and frequency f .

Then the FIM takes the form as [54–59]:

$$\begin{aligned} \Gamma_{ij} &= \sum_{\alpha} \left\langle \frac{\partial s_{\alpha}}{\partial \theta_i} \middle| \frac{\partial s_{\alpha}}{\partial \theta_j} \right\rangle \\ &= \sum_{\alpha} \left[\frac{2}{S_n(f_0)} \left(\int_{-\infty}^{\infty} \partial_i s_{\alpha}(t) \partial_j s_{\alpha}^*(t) dt \right) \right], \end{aligned} \quad (15)$$

in which θ_i denotes the i -th parameter and $\partial_i s_{\alpha} = \partial s_{\alpha} / \partial \theta_i$. Accordingly, the corresponding covariance matrix is given by

$$\sigma_{ij} = \langle \Delta \theta_i \Delta \theta_j \rangle \approx (\Gamma^{-1})_{ij}. \quad (16)$$

The $S_n(f)$ is the single-link noise power spectral density, which we will discuss in the next section. The angular uncertainty in sky localization is quantified as

$$\Delta \Omega_s = 2\pi |\cos \theta_s| \sqrt{\sigma_{\theta_s \theta_s} \sigma_{\phi_s \phi_s} - \sigma_{\theta_s \phi_s}^2}, \quad (17)$$

with θ_s and ϕ_s denoting the source sky coordinates. We now have the basic setup for the sky map resolution, and we will present numerical results in the next section.

III. SOURCE LOCALIZATION

The Crater Interferometry Gravitational-wave Observatory (CIGO) is a proposed equilateral-triangle laser interferometer designed to probe mid-frequency gravitational waves in the deci-hertz to 10-hertz range. Each arm has a nominal length of approximately 10^2 km, aiming for a target strain sensitivity of $\sim 10^{-24}$.

We evaluate the angular-localization accuracy of CIGO and compare it with two representative space-based detectors to assess its performance. LISA and TianQin, which adopt similar triangular configurations. LISA consists of three spacecraft forming a triangle with 2.5×10^6 km arm lengths, trailing Earth by about 20° in the ecliptic plane with an orbital plane inclined at 60° . While TianQin has arm lengths of 1.73×10^5 km and its normal vector of the detector plane points to RX J0806.3+1527 with the latitude $\theta_{tq} = -4.7^\circ$ and the longitude $\phi_{tq} = 120.5^\circ$ in heliocentric coordinates. Both detectors operate in an Earth-centered orbit.

The distinct orbital dynamics and orientations of these missions introduce different levels of amplitude and Doppler modulation in their detector responses [54, 56], which, in turn, strongly influence their sky-localization capabilities. By comparing the sky maps of angular resolution across these three detectors in the mid-frequency band, we can clearly identify the optimal operating frequency range and relative advantages of CIGO.

In this section, we adopt the FIM method described above, simulate 3600 gravitational-wave sources uniformly distributed across the sky, and compute angular-resolution sky maps for CIGO, LISA, and TianQin. We set the mission time to one year and the observation coverage to $-\pi/2 < \theta_s < \pi/2$ in latitude and $-\pi < \phi_s < \pi$ in longitude. The gravitational-wave signals are modeled as monochromatic waves, characterized by a simple waveform and a minimal set of parameters. To ensure the detectability of all signal sources, we set the SNR for all sources to 7.

The results of angular resolutions at the frequencies $f = 10^{-1}$ Hz, 1 Hz and 10 Hz for the LISA, Tianqin and CIGO are shown in Fig.2 and Fig.3. We show the sky map of the angular resolution for LISA, Tianqin and CIGO in

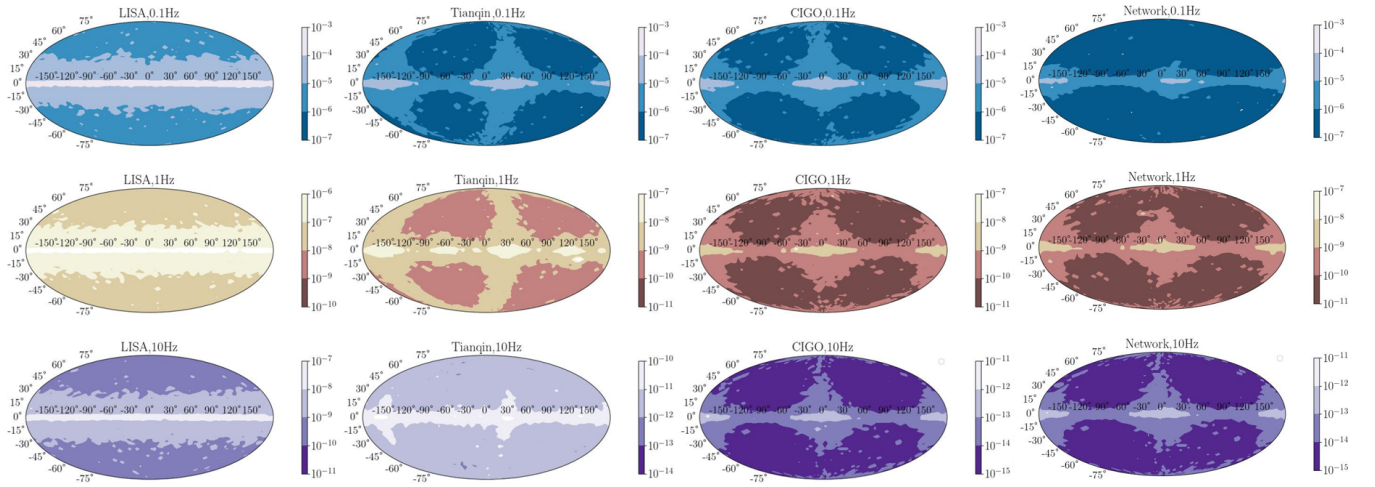


FIG. 2. The sky map of angular resolutions $\Delta\Omega_S$ of sources from different directions in the unit of steradian (1 steradian is 3000 square degrees) for LISA, Tianqin, CIGO, and their network. The horizontal axis represents the longitude ϕ_s and the vertical axis represents the latitude θ_s . The frequencies of monochromatic sources are 0.1 Hz, 1 Hz, and 10 Hz.

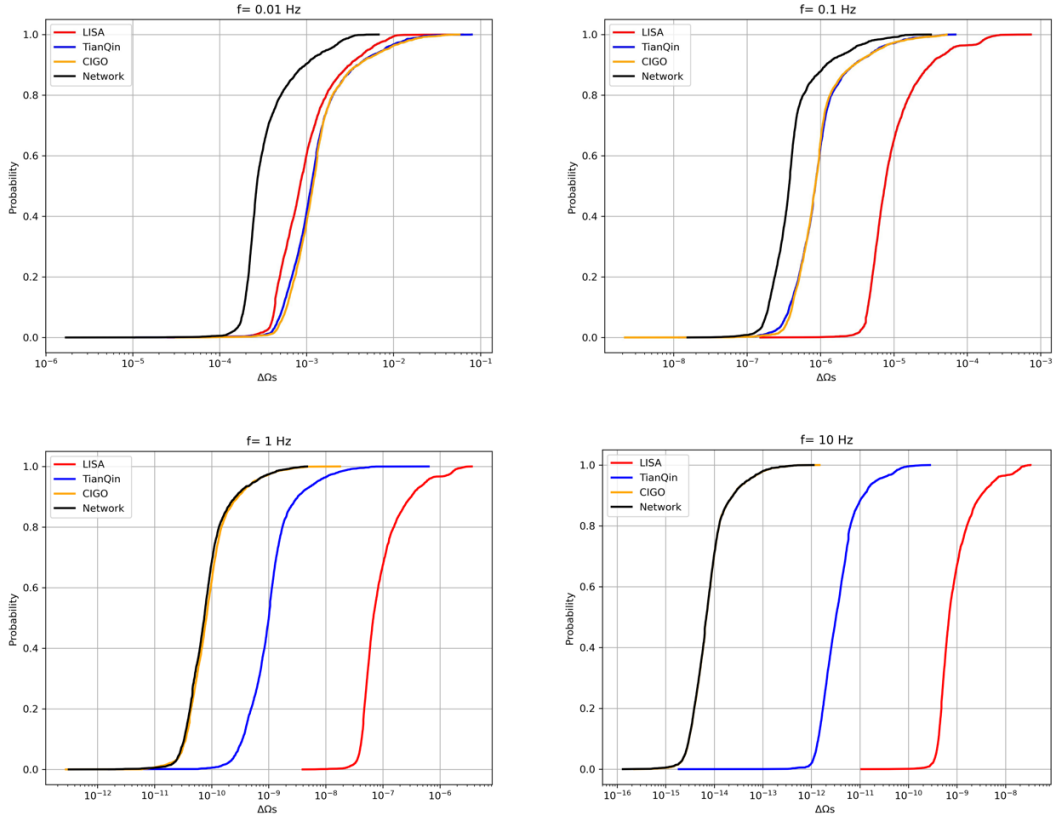


FIG. 3. Cumulative histograms of sky localization estimations $\Delta\Omega_S$ for different detectors

Fig.2, and the cumulative histograms of the angular resolution in Fig.3. The mean values of angular resolutions are summarized in Table I.

Fig.2 presents the sky maps of angular resolution for 3600 monochromatic gravitational-wave sources uniformly distributed over the celestial sphere, computed for LISA, TianQin, CIGO and their network at frequencies of 0.1 Hz, 1 Hz, and 10 Hz. The horizontal and vertical axes correspond to the source longitude (-180° to 180°) and latitude (-90° to 90°), respectively. The color scale represents the localization uncertainty $\Delta\Omega_s$ in steradians (sr), where

darker regions indicate better (smaller) angular resolution and lighter areas correspond to poorer performance. From top to bottom, the rows correspond to increasing frequencies (0.1 Hz, 1 Hz, and 10 Hz), while each column corresponds to a specific detector: LISA (left), TianQin (middle), and CIGO (right).

For LISA, we find that at all frequencies, the localization accuracy $\Delta\Omega_s$ for sources near the ecliptic plane is typically two orders of magnitude worse than that for sources near the poles. In contrast, TianQin shows degraded angular resolution for sources located along its detector plane (around $\phi_s \approx -150^\circ$ and 30°) and near the heliocentric equatorial plane, where $\Delta\Omega_s$ is roughly two orders of magnitude larger than in other sky regions. Similarly, for CIGO, the localization accuracy deteriorates by about one order of magnitude for sources located near the longitude $\phi_s = 5^\circ$ and 180° , as well as near the lunar equatorial plane.

These patterns arise from the differences in the orbital geometry and orientation of the detector planes. TianQin's detector usually continuously points toward its reference source RX J0806.3+1527, located at latitude $\theta = -4.7^\circ$ and longitude $\phi = 120.5^\circ$. CIGO, in contrast, is fixed on the lunar surface near the north pole, where the lunar spin axis is nearly parallel to the normal of the ecliptic plane, and the inclination between the lunar equator and the ecliptic (the so-called white-plane inclination) is about 5° . Consequently, CIGO's detector plane faces approximately toward $\theta = 5^\circ$. Along the detector-plane normal vector, the signal-to-noise ratio is significantly reduced, leading to reduced localization accuracy (larger $\Delta\Omega_s$) and weaker modulation. LISA, however, lacks a fixed reference source; its detector plane rotates around the Sun with an inclination of 60° , producing strong amplitude and Doppler modulations that significantly enhance sky-localization performance across most directions[57]. As a result, LISA exhibits a more uniform angular resolution over the sky map. At the same time, TianQin and CIGO show slightly less sky coverage, characterized by high precision over large regions but weaker performance in specific, limited directions.

Fig.3 illustrates the cumulative distribution functions (CDFs) of the angular resolution $\Delta\Omega_s$ for the same set of sources across different frequencies, with curves for LISA (red), TianQin (blue), CIGO (yellow), and their combined network (black). The x -axis is logarithmic in $\Delta\Omega_s$ (sr), and the y -axis shows the cumulative probability, i.e., the fraction of sources localized below a given uncertainty. The panels are arranged by frequency: left for 0.1 Hz, middle for 1 Hz, and right for 10 Hz.

At $f = 0.1$ Hz, both CIGO and TianQin exhibit localization accuracies of $\Delta\Omega_s \sim 10^{-6}$ sr, whereas LISA's resolution is reduced by roughly one order of magnitude. As the frequency increases to 10 Hz, CIGO's localization performance surpasses that of the other two detectors by more than two orders of magnitude. However, in our target band (0.1–10 Hz), the observing frequency satisfies $f \ll f^* = c/(2\pi L)$, the angular resolution $\Delta\Omega_s$ of a single detector improves with increasing gravitational-wave frequency. In contrast, for LISA ($f^* \simeq 0.02$ Hz) and TianQin ($f^* \simeq 0.28$ Hz), the target band lies well above their frequencies. Consequently, the transfer function's frequency dependence deteriorates markedly, causing the responses of LISA and TianQin to saturate.

For the network configuration combining CIGO, TianQin, and LISA, the joint observations provide a clear improvement at low frequencies ($f = 0.01$ – 0.1 Hz) when compared to any single detector. In this regime, the cumulative distributions of $\Delta\Omega_s$ shift leftward relative to the individual-detector curves, reflecting the benefit of the geometric complementarity among the three non-coplanar constellations.

As the frequency increases into the 1–10 Hz range, however, the network's performance becomes overwhelmingly dominated by CIGO. As indicated by the black CDF curve in Figure 3, the network curve coincides with that of CIGO at these frequencies, showing that CIGO's response effectively sets the localization accuracy of the joint observation. In this high-frequency regime, the contributions from LISA and TianQin become negligible, and the network inherits CIGO's superior angular-resolution capability.

f (Hz)	LISA	TianQin	CIGO	Network
	Mean value of angular resolution			
0.01	1.874×10^{-3}	2.633×10^{-3}	2.845×10^{-3}	5.783×10^{-4}
0.1	2.376×10^{-5}	2.250×10^{-6}	2.296×10^{-6}	9.221×10^{-7}
1	2.266×10^{-7}	2.930×10^{-9}	2.272×10^{-10}	1.967×10^{-10}
10	2.350×10^{-9}	8.719×10^{-12}	1.969×10^{-14}	1.927×10^{-14}

TABLE I. Angular resolution (in steradians) comparison for LISA, TianQin, CIGO, and their combined network at different frequencies.

For Michelson interferometers operating in space, such as TianQin and LISA, the analytical form of the single-link noise power spectral density is written as [60–62]

$$S_n(f) = \frac{S_x}{L^2} + \frac{4S_a}{(2\pi f)^4 L^2} \left(1 + \frac{10^{-4} \text{ Hz}}{f} \right), \quad (18)$$

where L denotes the interferometer arm length, $S_x^{1/2}$ and $S_a^{1/2}$ are displacement noise and acceleration noise, respectively. Since there is currently no formula for estimating quantum noise for a CIGO-like detector, which is a Michelson-laser interferometer operating on a planet, in this work, we first naively assume that the noise level of CIGO can be achieved at least at the noise level in TianQin [57] with the same frequency dependence.

One notable feature is that the CIGO detector is designed as a Michelson-laser interferometer deployed on the lunar surface. If we examine the detector's noise budget more closely, CIGO's performance can vary significantly with noise level. Notice that the formalism of Michelson-laser power spectral density is largely implementation-agnostic, so it is also suitable for CIGO [63, 64]. Here, we estimate the noise based on the ground-based program. Given that CIGO is deployed on the moon, it will be affected by the lunar environment, to assess for these effects, we employ the `pygwinc` package [65] and assume that CIGO adopts detector technologies comparable to those of the Cosmic Explorer Stage 1 (CE1) [66], including the test masses, thermal shielding, and vibration isolation systems, *etc.* Starting from the CE1 design noise budget, we modify the environmental parameters correspond to lunar conditions and obtain the corresponding lunar environmental strain noise. Following Ref. [63, 64], we adopt the relation below to connect the noise power spectral density $S_n(f)$ and the strain $h_n(f)$:

$$S_n(f) = |h_n(f)|^2 \quad (19)$$

Substituting into equation (17), we obtain the overall strain-noise budget, shown in Fig. 4. For instructions on setting and modifying the relevant parameters, please refer to Appendix B. As shown in Fig. 4, within the target frequency

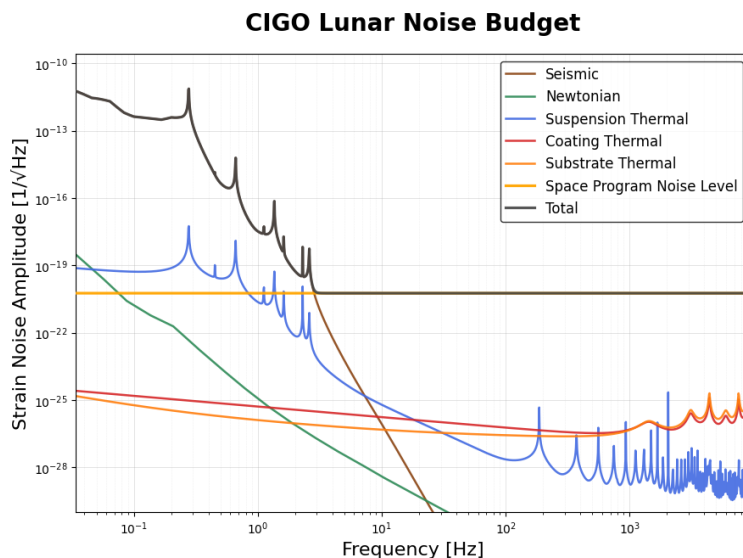


FIG. 4. Noise level estimation of CIGO

band (0.1-10Hz) of CIGO, if we assume that the overall sensitivity level of CIGO is comparable to that of CE1, then even though the lunar seismic environment is quieter than that on Earth, the total noise curve is still significantly elevated in the frequency range below 2.87Hz due to seismic noise contributions. Applying power-law fitting and smoothing procedure [42, 58, 67], we obtain an analytical expression for the noise strain amplitude for CIGO below:

$$h(f) = \begin{cases} 5.57 \times 10^{-15} f^{-2.15}, & 0.01 < f < 0.25 \text{ Hz}, \\ 1.12 \times 10^{-17} f^{-7.08}, & 2.15 < f < 2.87 \text{ Hz}, \\ \sqrt{S_n(f)}, & f > 2.87 \text{ Hz}. \end{cases} \quad (20)$$

By replacing Eq. (17) with Eq. (20), we recompute the angular resolution of CIGO, and the cumulative distribution histograms of the angular resolution are shown in Fig. 5.

Fig. 5 shows the cumulative histograms of the angular resolution $\Delta\Omega_s$ at 0.1 and 1Hz after accounting for lunar noise. It's seen that within the seismic-dominated frequency range of 0.1–2.87 Hz, the angular resolution of CIGO is substantially reduced. This indicates that, for a lunar-based implementation of CIGO, more advanced seismic isolation techniques and improved suspension thermal-noise suppression will be required to reduce instrumental noise further and achieve the localization performance demonstrated in Fig. 3.

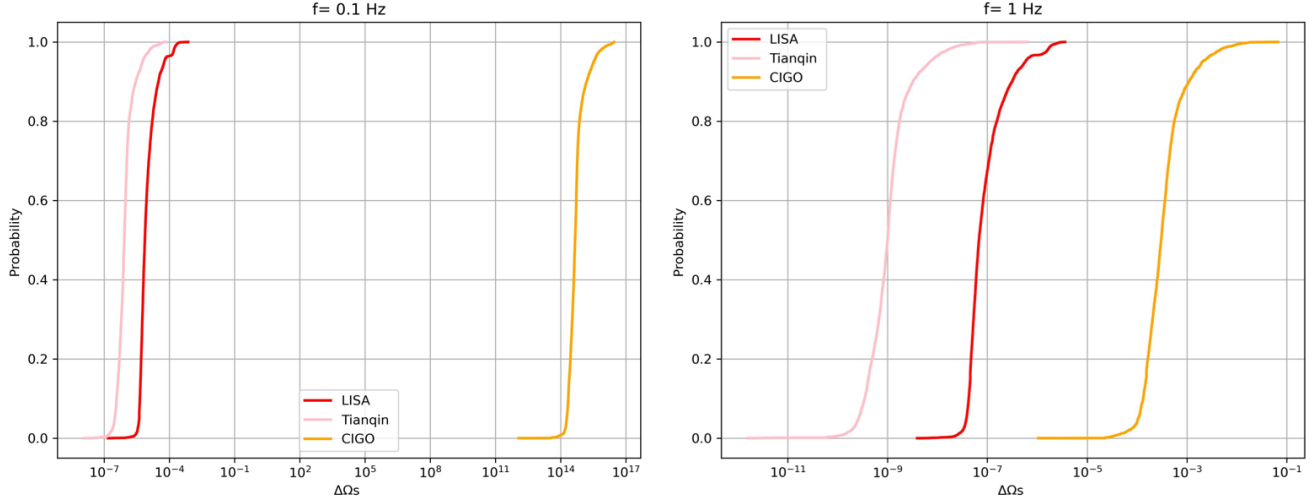


FIG. 5. Cumulative histograms of sky localization estimations $\Delta\Omega_S$ considering the lunar noise

IV. TETRAHEDRON FORM OF CIGO

In this section, we consider an upgraded configuration of the CIGO detector, referred to as the *Tetrahedron Crater Interferometry Gravitational-wave Observatory* (TCIGO). As illustrated in Fig. 3, we augment the original lunar-polar CIGO by adding an interferometric station at the bottom of the crater. The four stations form a regular tetrahedral geometry. Each triangular face functions effectively as two independent laser interferometers, introducing three additional baselines with distinct orientations. Consequently, a single observation can be treated as an eight-interferometer network. This configuration is proposed to improve sky-localization performance for lunar-based detectors.

We label the four interferometric stations as SC1–SC4. Following the orbital prescription of CIGO and adopting the trajectory settings of [68, 69], the position functions of the n -th detector are identical to Eqs. (10)–(13), which we reproduce here for completeness.

$$\begin{aligned}
X_n(t) &= R \sin \theta_c \cos \alpha_n(t) + R_M \cos \alpha_M(t) + R_E \cos \alpha_E(t) \\
&\quad + \frac{1}{2} e_1 R_M [\cos(2\alpha_M(t)) - 3] - \frac{3}{2} e_1^2 R_M \sin^2 \alpha_M(t) \cos \alpha_M(t) \\
&\quad + \frac{1}{2} e_2 R_E [\cos(2\alpha_E(t)) - 3] - \frac{3}{2} e_2^2 R_E \sin^2 \alpha_E(t) \cos \alpha_E(t) \\
&\quad + \mathcal{O}(3),
\end{aligned} \tag{21}$$

$$\begin{aligned}
Y_n(t) &= \left[R \sin \theta_c \sin \alpha_n(t) + R_M \sin \alpha_M(t) + \frac{1}{2} e_1 R_M \sin(2\alpha_M(t)) \right. \\
&\quad \left. + \frac{1}{2} e_1^2 R_M (3 \cos 2\alpha_M(t) - 1) \sin \alpha_M(t) \right] \sin \theta_m \\
&\quad + \left[R \cos \theta_c + R_E \sin \alpha_E(t) + \frac{1}{2} e_2 R_E \sin 2\alpha_E(t) \right. \\
&\quad \left. + \frac{1}{2} e_2^2 R_E (3 \cos(2\alpha_E(t)) - 1) \sin \alpha_E(t) \right] \cos \theta_+ \mathcal{O}(3),
\end{aligned} \tag{22}$$

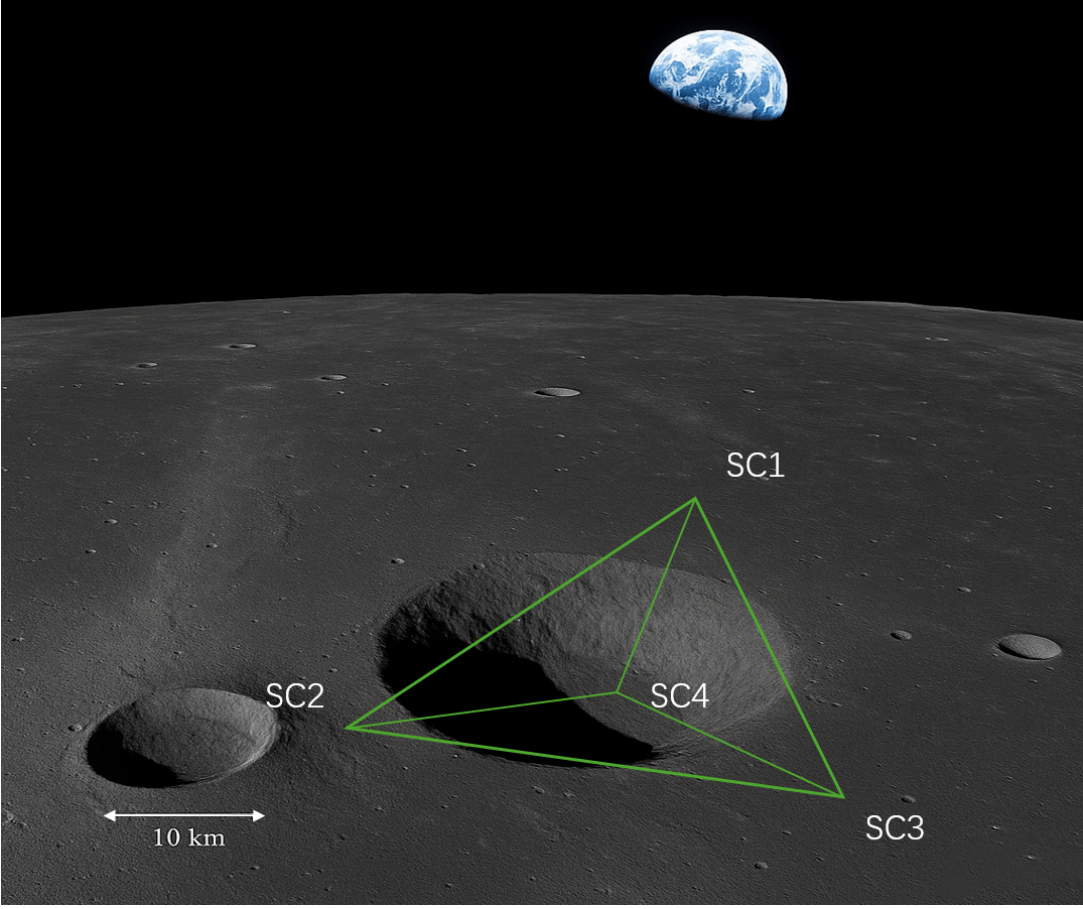


FIG. 6. **Conceptual design of TCIGO.** Three spacecraft (SC1–SC3) are situated on the rim of a lunar crater, with a fourth (SC4) located at its bottom, forming a regular tetrahedral configuration. Each end station, separated by 70 km, houses a test mass and three laser systems.

$$\begin{aligned}
 Z_n(t) = & R \sin \theta_m \cos \theta_c \\
 & - \left[R \sin \theta_c \sin \alpha_n(t) + R_M \sin \alpha_M(t) + \frac{1}{2} e_1 R_M \sin 2\alpha_M(t) \right. \\
 & \left. + \frac{1}{2} e_1^2 R_M (3 \cos 2\alpha_M(t) - 1) \sin \alpha_M(t) \right] \cos \theta_m + \mathcal{O}(3),
 \end{aligned} \tag{23}$$

The parameter R denotes the radius of the moon. L is the distance from the center of the detector array to each detector. L is the distance from the center of the detector to each detector. For SC1–SC3, we use $L = 40$ km, while for SC4, we take $L = 57.16$ km, such that the four stations form a regular tetrahedron. The angle $\alpha_n(t) = 2\pi f_n t + \kappa_n$ represents the angular displacement of the n -th detector in the detector-plane / lunar-polar coordinate system, with $\kappa_n = 2\pi(n-1)/3$, ($n = 1, 2, 3, 3.5$) characterizing the relative phase between SC1 and SC4. All other parameters follow Sec . 2.2.

We refer to the triangular detector formed by SC1–SC2–SC4 as $S1$ and that formed by SC1–SC3–SC4 as $S2$. The original CIGO corresponds to the triangle SC1–SC2–SC3. Figure 5 presents the sky maps of angular-resolution performance for 3600 monochromatic gravitational-wave sources uniformly distributed over the celestial sphere for $S1$ (left), CIGO (middle), and TCIGO (right), evaluated at frequencies of 0.1 Hz, 1 Hz, and 10 Hz. Figure 6 shows the cumulative distribution functions (CDFs) of the angular resolution $\Delta\Omega_s$ for the same set of sources across all frequencies, with curves for LISA (red), $S1$ (blue), $S2$ (pink; nearly overlapping with $S1$), CIGO (yellow), and TCIGO (purple).

From Fig. 6, we observe that for a single detector formed with SC4 (e.g., $S1$), the sky-localization distribution and precision are comparable to those of CIGO. However, its high-precision region is slightly smaller. However, when all four faces are combined to form the full TCIGO array, the reduction in angular resolution caused by the orientation of the CIGO (latitude $\theta = 5$) was compensated. As seen in Fig. 6, at $f = 0.1$ Hz, the cumulative localization performance

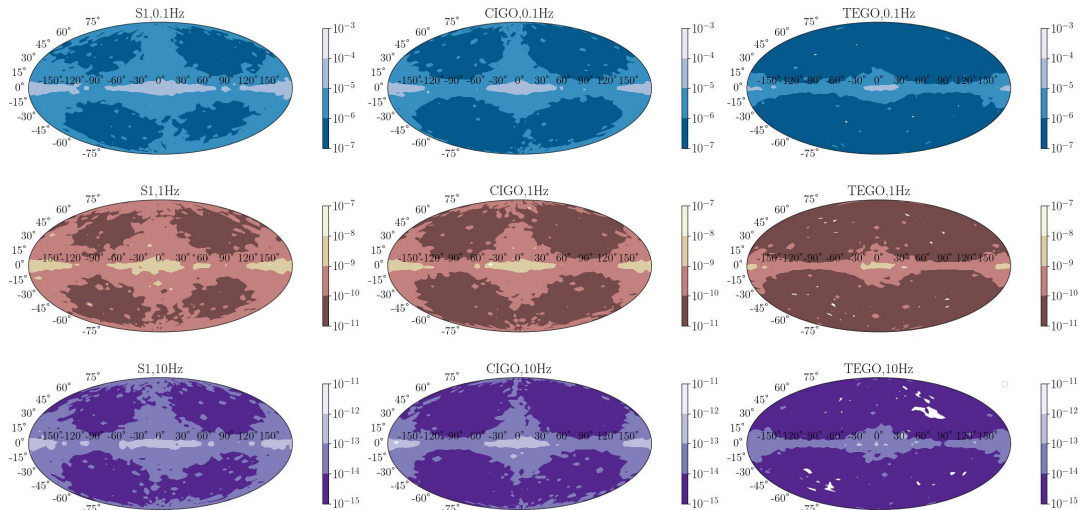


FIG. 7. The sky map of angular resolutions $\Delta\Omega_s$ of sources from different directions in the unit of steradian (1 steradian is 3000 square degrees) for S1, CIGO, and TCIGO. The horizontal axis represents the longitude ϕ_s and the vertical axis represents the latitude θ_s . The left panel shows S1, the middle panel shows CIGO, and the right panel shows TCIGO. From top to bottom, the frequencies of monochromatic sources are 0.1 Hz, 1 Hz, and 10 Hz.

of TCIGO is already comparable to the CIGO + space-based network configuration shown in Fig. 3. For $f > 0.1$ Hz, TCIGO surpasses not only CIGO but also all existing or planned space-based interferometers. Overall, within our target frequency band, TCIGO improves the angular resolution by a factor of 5 compared to CIGO.

V. CONCLUSION

We investigated the angular resolution of LISA, TianQin, and CIGO for monochromatic gravitational waves in the frequency band 0.1–10 Hz. The results show that CIGO exhibits excellent source-localization capability. At 0.1 Hz, CIGO performs comparably to TianQin. However, for $f > 0.1$ Hz, CIGO’s angular resolution surpasses that of TianQin and LISA by several orders of magnitude, and the joint localization performance of the three-detector network is dominated by CIGO. Similar to TianQin, the normal vector to the CIGO detector plane is aligned with the lunar north pole and thus points toward the exact ecliptic longitude on the sky; in this direction, the signal-to-noise ratio is significantly reduced, resulting in reduced localization accuracy (larger $\Delta\Omega_s$) and weak amplitude/phase modulation. Consequently, in the sky maps, the region around ecliptic longitude $\phi_s = 5^\circ$ exhibits noticeably lower angular resolution than other regions. In contrast, LISA benefits from continuously rotating detector-plane orientation along its orbit, which provides amplitude modulation and yields more uniform sky coverage. In addition, we investigate the impact of the detector-noise formalism on angular-resolution modeling and show that CIGO would achieve better performance if low-frequency lunar seismic noise is further suppressed.

To eliminate the angular-resolution blind spot caused by CIGO’s fixed orientation, we further placed an additional detector at the bottom of the same lunar crater. Together with the original three CIGO detectors, this forms a regular tetrahedral configuration. The tetrahedral geometry introduces three additional oriented planes, yielding six new independent interferometric channels. The results show that, across the observed frequency band, the angular resolution of each new detector alone is slightly lower than that of the original CIGO triad. However, when combined with the original detectors, the overall localization accuracy improves by a factor of approximately 5. Moreover, because the detector orientations now provide complete sky coverage, the sky coverage blind spots previously present in CIGO are effectively eliminated.

The lunar-based CIGO, particularly in its tetrahedral configuration, delivers outstanding localization performance for mid-frequency gravitational-wave sources in the 0.1–10 Hz band. It thereby serves as a vital bridge between space-based detectors (LISA, TianQin, Taiji), which dominate the low-frequency regime (10^{-4} – 10^{-1} Hz), and ground-based observatories (LIGO, Virgo, KAGRA, Einstein Telescope, Cosmic Explorer), which cover the high-frequency band (10 – 2×10^4 Hz). This unique setup makes CIGO an indispensable component of gravitational-wave astronomy in the coming decades

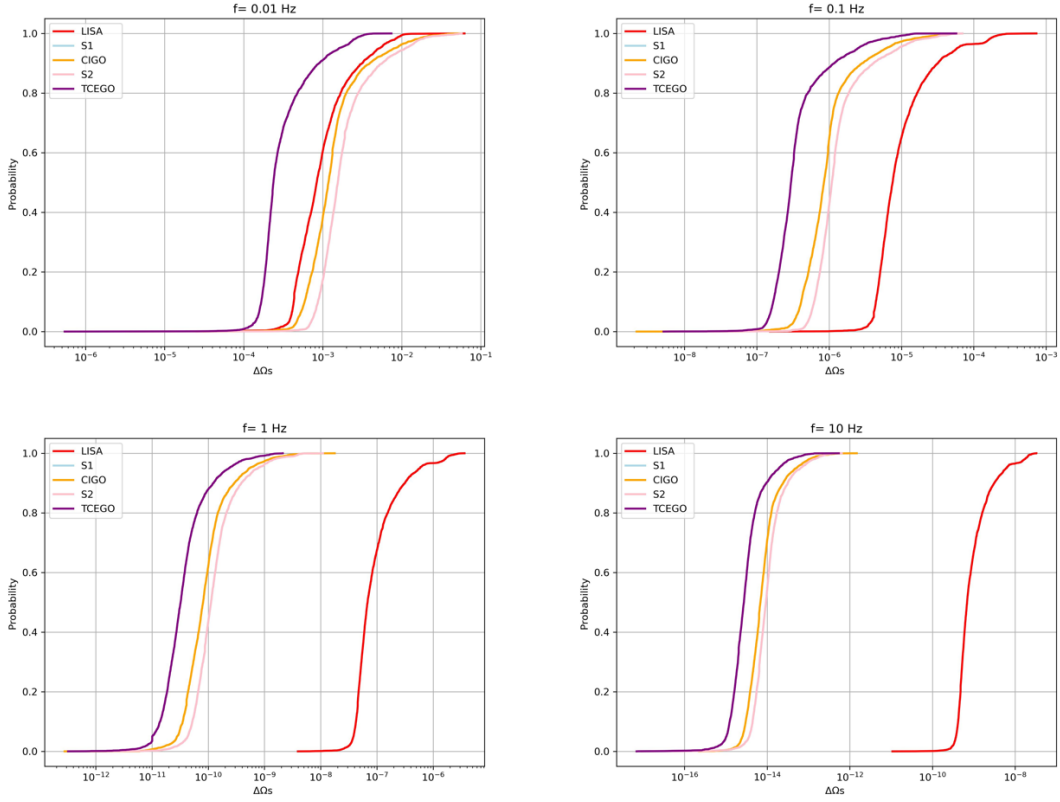


FIG. 8. Cumulative histograms of sky localization estimations $\Delta\Omega_S$ for different detectors

Appendix A: Derivation of the Detector Position in the Heliocentric–Ecliptic Coordinate System

In this appendix, we refer to the method in ref.[55] and [70] to derive the position vector of each detector in the heliocentric–ecliptic coordinate system by successively transforming from the detector frame to the lunar frame, and finally to the heliocentric frame.

1. Detector position in the lunar-centered frame

We first consider a coordinate system centered at the Moon, with the polar axis aligned with the lunar rotation axis. In this frame, each detector undergoes uniform circular motion around the polar axis. The position vector of the n -th detector is given by

$$\begin{aligned} x_n(t) &= R \sin \theta_c \cos \alpha_n(t), \\ y_n(t) &= R \sin \theta_c \sin \alpha_n(t), \\ z_n(t) &= R \cos \theta_c, \end{aligned} \tag{A1}$$

where $\alpha_n(t) = 2\pi f_n t + \kappa_n$ is the angular displacement of the n -th detector in the detector plane, with $\kappa_n = 2\pi(n-1)/3$, $n \in \{1, 2, 3\}$. Here, R denotes the moon radius, and the opening angle θ_c satisfies

$$\sin \theta_c = L/R, \tag{A2}$$

where L is the distance from the center of the detector array to each detector.

2. Lunar orbital motion in the geocentric–lunar frame

Next, we introduce a geocentric–lunar coordinate system with the Earth’s center as the origin. The z -axis is taken to be parallel to the lunar polar axis, while the x – y plane coincides with the lunar orbital plane.

The orbital motion of the Moon around the Earth, expanded to second order in the orbital eccentricity e_1 , is described by

$$\begin{aligned} x_{\text{Moon}}(t) &= R_M \cos \alpha_M(t) + \frac{1}{2} e_1 R_M [\cos 2\alpha_M(t) - 3] - \frac{3}{2} e_1^2 R_M \cos \alpha_M(t) \sin^2 \alpha_M(t), \\ y_{\text{Moon}}(t) &= R_M \sin \alpha_M(t) + \frac{1}{2} e_1 R_M \sin 2\alpha_M(t) + \frac{1}{2} e_1^2 R_M \sin \alpha_M(t) [3 \cos 2\alpha_M(t) - 1], \\ z_{\text{Moon}}(t) &= 0. \end{aligned} \quad (\text{A3})$$

Here, R_M and e_1 are the semi-major axis and eccentricity of the Moon's orbit around the Earth, respectively. The orbital phase, $\alpha_M(t) = 2\pi f_M t + \kappa_M$, represents the mean lunar longitude, where f_M is the lunar orbital frequency and κ_M is the mean longitude at $t = 0$.

3. Earth's orbital motion in the heliocentric–ecliptic frame

We now return to the heliocentric–ecliptic coordinate system, in which the Sun is located at the origin and the x – y plane coincides with the ecliptic plane. The orbital motion of the Earth around the Sun is given by

$$\begin{aligned} x_{\text{Earth}}(t) &= R_E \cos \alpha_E(t) + \frac{1}{2} e_2 R_E [\cos 2\alpha_E(t) - 3] - \frac{3}{2} e_2^2 R_E \cos \alpha_E(t) \sin^2 \alpha_E(t), \\ y_{\text{Earth}}(t) &= R_E \sin \alpha_E(t) + \frac{1}{2} e_2 R_E \sin 2\alpha_E(t) + \frac{1}{2} e_2^2 R_E \sin \alpha_E(t) [3 \cos 2\alpha_E(t) - 1], \\ z_{\text{Earth}}(t) &= 0. \end{aligned} \quad (\text{A4})$$

Here, R_E and e_2 denote the semi-major axis and eccentricity of the Earth's orbit, respectively. The orbital phase is defined as $\alpha_E(t) = 2\pi f_E t + \kappa_E$, where f_E is the Earth's orbital frequency and κ_E is the mean ecliptic longitude measured from the vernal equinox at $t = 0$.

4. Rotation from the lunar orbital plane to the ecliptic plane

To account for the inclination between the lunar orbital plane and the ecliptic plane, we introduce a rotation matrix \mathbf{R} ,

$$\mathbf{R} = \begin{pmatrix} 1 & 0 & 0 \\ 0 & \sin \theta_m & \cos \theta_m \\ 0 & -\cos \theta_m & \sin \theta_m \end{pmatrix}, \quad (\text{A5})$$

where θ_m is the inclination angle between the lunar and ecliptic planes.

5. Total detector position in the heliocentric–ecliptic frame

Finally, the trajectory of the n -th detector in the heliocentric–ecliptic reference frame is obtained by summing the orbital coordinates as

$$\begin{pmatrix} X_n(t) \\ Y_n(t) \\ Z_n(t) \end{pmatrix} = \mathbf{R} \left[\begin{pmatrix} x_n(t) \\ y_n(t) \\ z_n(t) \end{pmatrix} + \begin{pmatrix} x_{\text{Moon}}(t) \\ y_{\text{Moon}}(t) \\ z_{\text{Moon}}(t) \end{pmatrix} \right] + \begin{pmatrix} x_{\text{Earth}}(t) \\ y_{\text{Earth}}(t) \\ z_{\text{Earth}}(t) \end{pmatrix}. \quad (\text{A6})$$

This is how formulas (10)–(12) are obtained.

Appendix B: Modification of lunar base noise parameters based on the pygwinc CE1 project

This appendix details the key parameter modifications applied in the GWINC simulation for the lunar-based CIGO 100 km laser interferometric gravitational-wave detector, relative to the standard CE1 configuration. These

changes are designed to reflect the unique advantages of the lunar environment, including extremely low seismic background, natural high vacuum, cryogenic potential (80 K in this study), longer baseline, and higher laser power.

The modifications were implemented with the `safe.set` function to generate the noise-budget curves presented in the main text.

Key changes include:

- Arm length increased to 100 km, with mirror radii of curvature scaled proportionally to maintain the stability.
- Overall and local temperatures reduced to 100 K to significantly suppress thermal noise (coating thermal noise, substrate thermal noise, and suspension thermal noise).
- Laser input power raised to 1 kW and test mass increased to optimize
- Atmospheric parameters set to extremely low values to simulate the lunar hard vacuum.
- Seismic and Newtonian noise parameters substantially reduced to reflect the seismically quiet lunar environment (absence of atmospheric density and other fluctuations).

A detailed setting table is provided in Table II.

TABLE II. Parameter Modifications for the Lunar CIGO 100 km Detector

Parameter Path	Modified Value	Description
Infrastructure.Length	100000	Arm length 100 km (original ~ 4 km)
Infrastructure.Temp	100	Overall environment temperature (cryogenic thermal noise reduction)
Suspension.Temp	100	Suspension temperature (cryogenic)
Materials.Substrate.Temp	100	Mirror substrate temperature (cryogenic)
Laser.Power	1000	Input laser power 1 kW (enabled by lunar vacuum and low temperature)
Materials.MassRadius	0.3	Mirror radius 30 cm (increased mass to reduce radiation pressure noise)
Materials.MassThickness	0.4	Mirror thickness 40 cm (increased mass)
TCS.SRCloss	0.00	SRC thermal loss (negligible thermal lensing at low temperature)
Site	Moon	Site identifier (label only)
KneeFrequency	0.01	Seismic knee frequency (earlier roll-off)
LowFrequencyLevel	e^{-13}	Low-frequency seismic level (~ 4 orders of magnitude below Earth)
Gamma	2.0	Roll-off steepness (faster decay)
Rho	1500	Lunar regolith density
Beta	0.0	Disable Newtonian noise (no atmospheric density fluctuations on Moon)
pWaveSpeed	4000	P-wave speed
sWaveSpeed	2000	S-wave speed
RayleighWaveSpeed	2000	Rayleigh wave speed
pWaveLevel	e^{-8}	Extremely low P-wave intensity
sWaveLevel	e^{-8}	Extremely low S-wave intensity
TestMassHeight	3.0	Test mass height (optimized for lunar deployment)
Omicron	100	Feedforward cancellation factor (maximized suppression)
AirPressure	e^{-12}	Atmospheric pressure (near zero to avoid division by zero)
AirDensity	e^{-15}	Air density
AirKinematicViscosity	0	Air kinematic viscosity
SoundSpeed	e^{-3}	Speed of sound (tiny non-zero value)
WindSpeed	0	Wind speed
Temperature	100	Atmospheric temperature (consistent with overall)
TempStructConst	0	Temperature structure constant
KolmEnergy1m	0	Kolmogorov turbulence energy
Optics.Curvature.ITM	$1934 \times (100000/3995)$	ITM radius of curvature (scaled with arm length for cavity stability)
Optics.Curvature.ETM	$2245 \times (100000/3995)$	ETM radius of curvature (scaled with arm length for cavity stability)

-
- [1] Yungui Gong, Jun Luo, and Bin Wang. Concepts and status of chinese space gravitational wave detection projects. *Nature Astronomy*, 5(9):881–889, 2021.
- [2] Matthew Bailes, Beverly K Berger, Peter R Brady, M Branchesi, Karsten Danzmann, M Evans, Kelly Holley-Bockelmann, BR Iyer, T Kajita, S Katsanevas, et al. Gravitational-wave physics and astronomy in the 2020s and 2030s. *Nature Reviews Physics*, 3(5):344–366, 2021.

- [3] Rong-Gen Cai, Zong-Kuan Guo, Bin Hu, Chang Liu, Youjun Lu, Wei-Tou Ni, Wen-Hong Ruan, Naoki Seto, Gang Wang, and Yue-Liang Wu. On networks of space-based gravitational-wave detectors. *Fundamental Research*, 4(5):1072–1085, 2024.
- [4] Benjamin P Abbott, Richard Abbott, Thomas D Abbott, Matthew R Abernathy, Fausto Acernese, Katherine Ackley, Carl Adams, Thomas Adams, Paolo Addesso, Rana X Adhikari, et al. Gw151226: observation of gravitational waves from a 22-solar-mass binary black hole coalescence. *Physical review letters*, 116(24):241103, 2016.
- [5] Benjamin P Abbott, Rich Abbott, Thomas D Abbott, Fausto Acernese, Kendall Ackley, Carl Adams, Thomas Adams, Paolo Addesso, Rana X Adhikari, Vaishali B Adya, et al. Gw170104: observation of a 50-solar-mass binary black hole coalescence at redshift 0.2. *Physical review letters*, 118(22):221101, 2017.
- [6] Benjamin P Abbott, Richard Abbott, TD Abbott, F Acernese, K Ackley, C Adams, T Adams, P Addesso, Rana X Adhikari, Vaishali B Adya, et al. Gw170814: a three-detector observation of gravitational waves from a binary black hole coalescence. *Physical review letters*, 119(14):141101, 2017.
- [7] Benjamin P Abbott, Richard Abbott, TD Abbott, F Acernese, K Ackley, C Adams, T Adams, P Addesso, Rana X Adhikari, Vaishali B Adya, et al. Gw170817: Measurements of neutron star radii and equation of state. *Physical review letters*, 121(16):161101, 2018.
- [8] Benjamin P Abbott, Rich Abbott, Thomas D Abbott, Fausto Acernese, Kendall Ackley, Carl Adams, Thomas Adams, Paolo Addesso, Rana X Adhikari, Vaishali B Adya, et al. Gw170817: observation of gravitational waves from a binary neutron star inspiral. *Physical review letters*, 119(16):161101, 2017.
- [9] Benjamin P Abbott, Richard Abbott, TDea Abbott, S Abraham, F Acernese, K Ackley, C Adams, RX Adhikari, VB Adya, Christoph Affeldt, et al. Gwtc-1: a gravitational-wave transient catalog of compact binary mergers observed by ligo and virgo during the first and second observing runs. *Physical Review X*, 9(3):031040, 2019.
- [10] Benjamin P Abbott, R Abbott, R Adhikari, P Ajith, Bruce Allen, G Allen, RS Amin, SB Anderson, WG Anderson, MA Arain, et al. Ligo: the laser interferometer gravitational-wave observatory. *Reports on Progress in physics*, 72(7):076901, 2009.
- [11] Benjamin P Abbott, Richard Abbott, Thomas D Abbott, Matthew R Abernathy, Fausto Acernese, Kendall Ackley, Carl Adams, Thomas Adams, Paolo Addesso, Rana X Adhikari, et al. Observation of gravitational waves from a binary black hole merger. *Physical review letters*, 116(6):061102, 2016.
- [12] Pau Amaro-Seoane, Heather Audley, Stanislav Babak, John Baker, Enrico Barausse, Peter Bender, Emanuele Berti, Pierre Binétruy, Michael Born, Daniele Bortoluzzi, et al. Laser interferometer space antenna. *arXiv preprint arXiv:1702.00786*, 2017.
- [13] European Space Agency. Summary of the laser interferometer space antenna (lisa) mission. <https://sci.esa.int/web/lisa/-/31380-summary>, 2025. ESA Science and Technology Summary.
- [14] Jun Luo, Li-Sheng Chen, Hui-Zong Duan, Yun-Gui Gong, Shoucun Hu, Jianghui Ji, Qi Liu, Jianwei Mei, Vadim Milyukov, Mikhail Sazhin, et al. Tianqin: a space-borne gravitational wave detector. *Classical and Quantum Gravity*, 33(3):035010, 2016.
- [15] Jun Luo, Shaojun Bai, Yanzheng Bai, Lin Cai, Hao Dang, Qijia Dong, Hui-Zong Duan, Yuanbo Du, Lei Fan, Xinju Fu, et al. Progress of the tianqin project. *Classical and Quantum Gravity*, 42(17):173001, 2025.
- [16] Wen-Rui Hu and Yue-Liang Wu. The taiji program in space for gravitational wave physics and the nature of gravity, 2017.
- [17] Ziren Luo, Yan Wang, Yueliang Wu, Wenrui Hu, and Gang Jin. The taiji program: A concise overview. *Progress of Theoretical and Experimental Physics*, 2021(5):05A108, 2021.
- [18] Kazuaki Kuroda, Wei-Tou Ni, and Wei-Ping Pan. Gravitational waves: Classification, methods of detection, sensitivities and sources. *International Journal of Modern Physics D*, 24(14):1530031, 2015.
- [19] Dongfeng Gao, Wei-Tou Ni, Jin Wang, Ming-Sheng Zhan, and Lin Zhou. Mid-frequency gravitational waves (0.1-10 hz): Sources and detection methods summary of the parallel session gw2 of mg16 meeting. *arXiv preprint arXiv:2111.09715*, 2021.
- [20] Manoel Felipe Sousa, Tabata Aira Ferreira, and Massimo Tinto. Parameter estimation precision with geocentric gravitational wave interferometers: Monochromatic signals. *Universe*, 11(4):122, 2025.
- [21] Tong Jiang, Yungui Gong, and Xuchen Lu. Sky localization of space-based detectors with time-delay interferometry. *Journal of Cosmology and Astroparticle Physics*, 2024(10):067, 2024.
- [22] Ivo R Seitenzahl, Matthias Herzog, Ashley J Ruiter, Kai Marquardt, Sebastian T Ohlmann, and Friedrich K Röpke. Neutrino and gravitational wave signal of a delayed-detonation model of type ia supernovae. *Physical Review D*, 92(12):124013, 2015.
- [23] Manuel Arca Sedda, Christopher PL Berry, Karan Jani, Pau Amaro-Seoane, Pierre Auclair, Jonathon Baird, Tessa Baker, Emanuele Berti, Katelyn Breivik, Adam Burrows, et al. The missing link in gravitational-wave astronomy: discoveries waiting in the decihertz range. *Classical and Quantum Gravity*, 37(21):215011, 2020.
- [24] Karan Jani, Deirdre Shoemaker, and Curt Cutler. Detectability of intermediate-mass black holes in multiband gravitational wave astronomy. *Nature Astronomy*, 4(3):260–265, 2020.
- [25] Run-Min Yao, Xiao-Jun Bi, Peng-Fei Yin, and Qing-Guo Huang. Axion-like dark matter search with space-based gravitational wave detectors. *arXiv preprint arXiv:2504.10083*, 2025.
- [26] Heng-Tao Xu, Yue-Hui Yao, Yong Tang, and Yue-Liang Wu. Distinguishing monochromatic signals in lisa and taiji: Ultralight dark matter versus gravitational waves. *Physical Review D*, 112(9):095021, 2025.
- [27] Ke Wang and Yin Zhong. Frequency modulation of gravitational waves by ultralight scalar dark matter. *Physical Review D*, 108(12):123531, 2023.
- [28] Marco Figliolia, Francesco Grippa, Gaetano Lambiase, and Luca Visinelli. Gravitational signatures of axion dark matter

- via parity-violating interactions. *arXiv preprint arXiv:2509.12038*, 2025.
- [29] Seiji Kawamura, Takashi Nakamura, Masaki Ando, Naoki Seto, Tomotada Akutsu, Ikkoh Funaki, Kunihito Ioka, Nobuyuki Kanda, Isao Kawano, Mitsuru Musha, et al. Space gravitational-wave antennas decigo and b-decigo. *International Journal of Modern Physics D*, 28(12):1845001, 2019.
- [30] Seiji Kawamura, Masaki Ando, Naoki Seto, Shuichi Sato, Mitsuru Musha, Isao Kawano, Jun'ichi Yokoyama, Takahiro Tanaka, Kunihito Ioka, Tomotada Akutsu, et al. Current status of space gravitational wave antenna decigo and b-decigo. *Progress of Theoretical and Experimental Physics*, 2021(5):05A105, 2021.
- [31] Sven Abend, Baptiste Allard, Iván Alonso, John Antoniadis, Henrique Araújo, Gianluigi Arduini, Aidan S Arnold, Tobias Asano, Nadja Augst, Leonardo Badurina, et al. Terrestrial very-long-baseline atom interferometry: Workshop summary. *AVS quantum science*, 6(2), 2024.
- [32] Jeff Crowder and Neil J Cornish. Beyond lisa: Exploring future gravitational wave missions. *Physical Review D—Particles, Fields, Gravitation, and Cosmology*, 72(8):083005, 2005.
- [33] Tomofumi Shimoda, Satoru Takano, Ching Pin Ooi, Naoki Aritomi, Yuta Michimura, Masaki Ando, and Ayaka Shoda. Torsion-bar antenna: A ground-based mid-frequency and low-frequency gravitational wave detector. *International Journal of Modern Physics D*, 29(04):1940003, 2020.
- [34] L Badurina, E Bentine, Diego Blas, K Bongs, D Bortoletto, T Bowcock, K Bridges, W Bowden, O Buchmueller, C Burrage, et al. Aion: an atom interferometer observatory and network. *Journal of Cosmology and Astroparticle Physics*, 2020(05):011, 2020.
- [35] Ming-Sheng Zhan, Jin Wang, Wei-Tou Ni, Dong-Feng Gao, Gang Wang, Ling-Xiang He, Run-Bing Li, Lin Zhou, Xi Chen, Jia-Qi Zhong, et al. Zaiga: Zhaoshan long-baseline atom interferometer gravitation antenna. *International Journal of Modern Physics D*, 29:1940005, 2020.
- [36] John Baker, Simon F Barke, Peter L Bender, Emanuele Berti, Robert Caldwell, John W Conklin, Neil Cornish, Elizabeth C Ferrara, Kelly Holley-Bockelmann, Brittany Kamai, et al. Space based gravitational wave astronomy beyond lisa. *arXiv preprint arXiv:1907.11305*, 2019.
- [37] Marica Branchesi, Maurizio Falanga, Jan Harms, Karan Jani, Stavros Katsanevas, Philippe Lognonné, Francesca Badaracco, Luigi Cacciapuoti, Enrico Cappellaro, Simone Dell'Agnello, et al. Lunar gravitational-wave detection. *Space Science Reviews*, 219(8):67, 2023.
- [38] Norman Lafave and Thomas L Wilson. Lunar ligo: A new concept in gravitational wave astronomy. In *Lunar and Planetary Inst., Twenty-Fourth Lunar and Planetary Science Conference. Part 2: GM*, 1993.
- [39] Cozzumbo Andrea, Mestichelli Benedetta, Mirabile Marco, Paiella Lavinia, Tissino Jacopo, and Harms Jan. Opportunities and limits of lunar gravitational-wave detection, 2023.
- [40] Hanlin Song, Han Yan, Yacheng Kang, Xian Chen, Junjie Zhao, and Lijing Shao. Probing intermediate-mass black hole binaries with the lunar gravitational-wave antenna. *npj Space Exploration*, 1(1):2, 2025.
- [41] Han Yan, Xian Chen, Jinhai Zhang, Fan Zhang, Mengyao Wang, and Lijing Shao. Toward a consistent calculation of the lunar response to gravitational waves. *Physical Review D*, 109(6):064092, 2024.
- [42] Karan Jani and Abraham Loeb. Gravitational-wave lunar observatory for cosmology. *Journal of Cosmology and Astroparticle Physics*, 2021(06):044, 2021.
- [43] Karan Jani, Matthew Abernathy, Emanuele Berti, Valerio Boschi, Sukanya Chakrabarti, Alice Cocoros, John W Conklin, Teviet Creighton, Simone Dell'Agnello, Jean-Claude Diels, et al. Laser interferometer lunar antenna (lila): Advancing the us priorities in gravitational-wave and lunar science. *arXiv preprint arXiv:2508.11631*, 2025.
- [44] Jan Harms, Filippo Ambrosino, Lorella Angelini, Valentina Braitto, Marica Branchesi, Enzo Brocato, Enrico Cappellaro, Eugenio Coccia, Michael Coughlin, Roberto Della Ceca, et al. Lunar gravitational-wave antenna. *The Astrophysical Journal*, 910(1):1, 2021.
- [45] Parameswaran Ajith, Pau Amaro Seoane, Manuel Arca Sedda, Riccardo Arcodia, Francesca Badaracco, Biswajit Banerjee, Enis Belgacem, Giovanni Benetti, Stefano Benetti, Alexey Bobrick, et al. The lunar gravitational-wave antenna: Mission studies and science case. *arXiv preprint arXiv:2404.09181*, 2024.
- [46] Francis S Johnson, James M Carroll, and Dallas E Evans. Vacuum measurements on the lunar surface. *Journal of Vacuum Science and Technology*, 9(1):450–456, 1972.
- [47] Jan Harms. Seismic background limitation of lunar gravitational-wave detectors. *Physical Review Letters*, 129(7):071102, 2022.
- [48] G De Angelis, FF Badavi, JM Clem, SR Blattnig, MS Cloudsley, JE Nealy, RK Tripathi, and JW Wilson. Modeling of the lunar radiation environment. *Nuclear Physics B—Proceedings Supplements*, 166:169–183, 2007.
- [49] M Horányi, JR Szalay, S Kempf, J Schmidt, E Grün, R Srama, and Z Sternovsky. A permanent, asymmetric dust cloud around the moon. *Nature*, 522(7556):324–326, 2015.
- [50] Eric Larose, Michel Campillo, A Khan, and Y Nakamura. Lunar subsurface investigated from correlation of seismic noise. *Geophysical Research Letters*, 32:L16201, 2005.
- [51] Philippe Lognonné, Mathieu Le Feuvre, Catherine L Johnson, and Renee C Weber. Moon meteoritic seismic hum: steady state prediction. *Journal of Geophysical Research: Planets*, 114(E12), 2009.
- [52] Djuna Lize Croon and David James Weir. Gravitational waves from phase transitions. *Contemporary Physics*, 65(2):75–96, 2024.
- [53] Ruiyu Zhou and Ligong Bian. Gravitational waves from cosmic strings after a first-order phase transition. *Chinese Physics C*, 46(4):043104, 2022.
- [54] Arkadiusz Blaüt. Accuracy of estimation of parameters with lisa. *Physical Review D—Particles, Fields, Gravitation, and Cosmology*, 83(8):083006, 2011.

- [55] Xin-Chun Hu, Xiao-Hong Li, Yan Wang, Wen-Fan Feng, Ming-Yue Zhou, Yi-Ming Hu, Shou-Cun Hu, Jian-Wei Mei, and Cheng-Gang Shao. Fundamentals of the orbit and response for tianqin. *Classical and Quantum Gravity*, 35(9):095008, 2018.
- [56] Curt Cutler. Angular resolution of the lisa gravitational wave detector. *Physical Review D*, 57(12):7089, 1998.
- [57] Chao Zhang, Yungui Gong, Hang Liu, Bin Wang, and Chunyu Zhang. Sky localization of space-based gravitational wave detectors. *Physical Review D*, 103(10):103013, 2021.
- [58] Neil J Cornish and Shane L Larson. Space missions to detect the cosmic gravitational-wave background. *Classical and Quantum Gravity*, 18(17):3473, 2001.
- [59] Chunyu Zhang, Yungui Gong, and Chao Zhang. Source localizations with the network of space-based gravitational wave detectors. *Physical Review D*, 106(2):024004, 2022.
- [60] Travis Robson, Neil J Cornish, and Chang Liu. The construction and use of lisa sensitivity curves. *Classical and Quantum Gravity*, 36(10):105011, 2019.
- [61] Babak Stanislav, Petiteau Antoine, and Hewitson Martin. Lisa sensitivity and snr calculations, 2021.
- [62] Neil J Cornish. Detecting a stochastic gravitational wave background with the laser interferometer space antenna. *Physical Review D*, 65(2):022004, 2001.
- [63] Bangalore Suryanarayana Sathyaprakash and Bernard F Schutz. Physics, astrophysics and cosmology with gravitational waves. *Living reviews in relativity*, 12(1):2, 2009.
- [64] Christopher J Moore, Robert H Cole, and Christopher PL Berry. Gravitational-wave sensitivity curves. *Classical and Quantum Gravity*, 32(1):015014, 2014.
- [65] LIGO Scientific Collaboration. pygwinc: Gravitational wave interferometer noise calculator, 2020. URL <https://git.ligo.org/gwinc/pygwinc>. Accessed: 2025-01-XX.
- [66] Evan D Hall. Cosmic explorer: A next-generation ground-based gravitational-wave observatory. *Galaxies*, 10(4):90, 2022.
- [67] Peter L Bender and Dieter Hils. Confusion noise level due to galactic and extragalactic binaries. *Classical and Quantum Gravity*, 14(6):1439, 1997.
- [68] Louis J Rubbo, Neil J Cornish, and Olivier Poujade. Forward modeling of space-borne gravitational wave detectors. *Physical Review D*, 69(8):082003, 2004.
- [69] Hong-Bo Jin and Cong-Feng Qiao. Tetrahedron constellation of gravitational wave observatory. *Science China Physics, Mechanics & Astronomy*, 68(2):220414, 2025.
- [70] Bofeng Wu, Chao-Guang Huang, and Cong-Feng Qiao. Analytical analysis on the orbits of taiji spacecrafts. *arXiv preprint arXiv:1907.06178*, 2019.